Check for updates

Advanced Functional Materials

ADVANCED FUNCTIONAL MATERIALS
www.afm-journal.de

RESEARCH ARTICLE

Highly Thermally Conductive and High Shear Strength Graphene Fiber Composites via Molecular Conjugation Interface Engineering for Extreme Thermal Management

Xiangyang Feng[1,2] | Weiwei Lou[3] | Guandong Wu[4] | Xin Ming[1] | Bo Wang[1] | Jiahao Lu[1] | Lei He[1] | Pengxiang Zhou[1] | Lu Chen[1] | Yingbo Yan[1] | Chendong Ge[1] | Shiqi Wu[1] | Xueyin Chen[1] | Peng Xu[1] | Fei Xing[5] | Ji Zhou[5] | Zhen Xu[1] | Zhongzhen Yu[6] | Wenfei Shen[2] | Jianguo Tang[2] | Lin Qiu[4] | Yingjun Liu[1] | Chao Gao[1]

[1]MOE Key Laboratory of Macromolecular Synthesis and Functionalization, Department of Polymer Science and Engineering, Department of Materials Science and Engineering, Zhejiang Key Laboratory of Advanced Organic Materials and Technologies, Research Center for Advanced Fibers, Zhejiang University, Hangzhou, China | [2]Institute of Hybrid Materials, National Center of International Joint Research for Hybrid Materials Technology, National Base of International Science & Technology Cooperation On Hybrid Materials, College of Materials Science and Engineering, Qingdao University, Qingdao, China | [3]College of Medicine, The First Affiliated Hospital, Zhejiang University, Hangzhou, China | [4]School of Energy and Environmental Engineering, University of Science and Technology Beijing, Beijing, China | [5]Beijing Institute of Space Mechanics & Electricity, Beijing, China | [6]State Key Laboratory of Organic-Inorganic Composites, College of Materials Science and Engineering, Beijing University of Chemical Technology, Beijing, China

Correspondence: Xin Ming (xin_ming@zju.edu.cn) | Wenfei Shen (shenwenfei@qdu.edu.cn) | Jianguo Tang (tang@qdu.edu.cn) | Lin Qiu (qiulin@ustb.edu.cn) | Yingjun Liu (yingjunliu@zju.edu.cn) | Chao Gao (chaogao@zju.edu.cn)

Received: 28 August 2025 | **Revised:** 14 December 2025 | **Accepted:** 19 December 2025

Keywords: fiber composite | graphene fiber | highly thermal conductivity | interfacial thermal conduction | molecular conjugation interface engineering

ABSTRACT

Highly thermally conductive graphene fibers (GFs) hold exceptional promise for next-generation high-flux thermal management systems, yet their integration into advanced composites remains fundamentally limited by insufficient interfacial compatibility with polymer resin. This limitation severely restricts both thermal and mechanical transfer efficiency and compromises stability under extreme thermal cycling. Herein, a molecularly tailored conjugation interfaces engineering through strategically selected silane-based molecular tethers grafted onto the wrinkled GF surfaces to establish covalent bridges into the epoxy network, effectively addressing the interfacial bonding dilemma between GFs and polymer resin is introduced. The resultant GF composites achieve a synergistic enhancement in interfacial shear strength increased by 61.6% (from 55.2 to 89.2 MPa) and a record-level in-plane thermal conductivity of 571.1 W m^{-1} K^{-1}. Critically, the thermal conductivity retention consistently exceeds 98% throughout 100 thermal shock cycles (25 to 125°C), confirming exceptional interfacial stability and thermal fatigue resistance. Furthermore, molecular dynamics (MD) simulations reveal that rigid benzene ring of molecular tethers interphase enables exceptional interfacial thermal conductance of 373.56 MW m^{-2} K^{-1} between graphene and epoxy, while flexible or mismatched molecular tethers agents induce disorder and weaken spectral coupling. This molecular conjugation interface engineering unlocks the interfacial design and chemistry for improving thermomechanical performances of GF composites, paving the way for robust and high-flux thermal management.

Xiangyang Feng, Weiwei Lou, and Guandong Wu contributed equally to this work.

© 2026 Wiley-VCH GmbH

1 | Introduction

Graphene fibers (GFs) as a new kind of carbonaceous fiber material since Gao's pioneering work in 2011, exhibit unparalleled multifunctionality with significant attention, combining lightweight, flexibility, high electrical conductivity (1.19×10^6 S m^{-1}) and superior thermal conductivity (up to 1660 W m^{-1} K^{-1}) [1–6]. These intrinsic properties position GFs as promising candidates for next-generation structural-functional integration materials. Importantly, while individual GF exhibits superior intrinsic thermal conductivity, the continuous fabrication of scalable GF bundles is an indispensable prerequisite for meeting industrial-scale demands in composite manufacturing [7–10]. Recently, extending from individual fiber excellence to industrial-scale production has been achieved through wet-spinning coupled with cascade hydroplastic-stretching strategy, enabling continuous fabrication of aligned 0.1K GF filaments [11]. The scaled GF bundles retain benchmark properties, including 1.4 GPa tensile strength, 4.1×10^5 S m^{-1} electrical conductivity and 1204 W m^{-1} K^{-1} thermal conductivity, which is far excess traditional PAN-based and Pitch-based carbon fibers (CFs) (Figure 1a) [9, 12]. Recently, Yu et al. reported CF-based composites with thermal conductivities as high as 289.5 W m^{-1} K^{-1} via a bionic bamboo stem array-leaf heat conduction network, reaching metal-level performance. Sun et al. have also achieved interfacial shear strengths surpassing 70 MPa via in situ grown vertical carbon nanosheets [13–16]. Building on these advances, CF-based composites exhibit great application in the thermal management field [17–21]. Nevertheless, the thermal performance of CF-reinforced composites is often bottlenecked by the relatively low intrinsic thermal conductivity of carbon fibers and their smooth, chemically inert surfaces, which hinder effective interfacial modification [22–24]. In contrast, GFs combine superior intrinsic thermal conductivity with a naturally wrinkled surface that could facilitate thermal and mechanical performances. Besides, the manufacturability breakthrough of GFs bridges laboratory innovation to industrial-scale applications, enabling their integration into large-scale fiber-reinforced composites for aerospace, energy, and high-flux thermal management applications [11, 25, 26].

Highly thermally conductive graphene-based fillers have demonstrated promise for thermal management composites, with one-dimensional fibrous architectures representing a critical yet underexplored paradigm [27–30]. The pristine GF-based polymer composites fabricated via the direct implementation and hot-pressing method exhibit thermal conductivity up to 553 W m^{-1} K^{-1}, outperforming traditional metal materials [28]. However, these high-performance GFs in macroscopic composites still necessitate deliberate interfaces engineering to optimize the boundary phase and interactions between the GFs and epoxy, which is a challenge amplified by the typical structural features of GFs [2, 31, 32]. Unlike conventional CFs, the highly thermally conductive GFs feature crystallographic anisotropy with large and low-defect graphitic domains and surface topology with distinctive hierarchical wrinkles (100 to 500 nm) [2, 33]. These unique structures differ fundamentally from conventional CFs, necessitating tailored interface design. The critical role of interfacial bonding in determining composite performance is well-established for traditional carbonaceous fibers. However, these microstructural distinctions necessitate exploring rather than directly adopting traditional CF modification protocols, including sizing, oxidation grafting, chemical deposition, and plasma treatment [34–43]. These methods provide useful guidance for the interface design engineering of GFs. These inherent microstructural features of GFs pose fundamental interfacial design challenges, which hinder realizing full thermal management potential of GF composites in the precise regulation of interfacial interactions.

Here, we propose a molecular-conjugation interfaces engineering to address the fundamental interfacial incompatibility for highly thermal conductivity and mechanically strong GF composites. Through constructing covalent bridge interphase using optimized silane molecular tethers, the modified GF composites achieve synergistic thermomechanical performance enhancements, with the interfacial shear strength (IFSS) reaching 89.2 MPa (61.6% increase) and the in-plane thermal conductivity attaining 571.1 W m^{-1} K^{-1} (Figure 1b). Additionally, the robust conjugated molecular interphase maintains over 98% thermal conductivity retention even after 100 thermal shock cycles (25 to 125°C) through stable structures of GF composites. The MD simulations reveal that the molecular conjugation interfaces between graphene and benzene-ring tethers facilitate directional phonon transport channels to bypass traditional interfacial scattering barriers, resulting in an interfacial thermal conductance (ITC) up to 373.56 MW m^{-2} K^{-1}. Meanwhile, the wrinkle-adaptive anchoring morphology enhances mechanical interlocking, ensuring the performance stability. Our work establishes a new conjugation framework and offers new insights for optimizing and designing the inherent thermal-mechanical coupling interfaces in the GF-based polymer composites, providing a feasible pathway for thermal management materials operating under high heat flux conditions of extreme thermal protection and power electronics cooling.

2 | Result and Discussion

2.1 | Fabrication and Characterization of GF Composites via Molecular Conjugation Interface Engineering

The fabrication process of the GF composites is shown in Figure 1c, where the flexible GF bundles (Figure 1d) were first combined into a thick fiber bundle, then sequentially subjected to plasma treatment, silane coupling agent (SCA) reaction, ethanol cleaning, and epoxy (EP) impregnation (Figure 1e), finally molded into the composite material through hot pressing (Figure 1f). The reaction mechanism is detailed in Figure 1g, with the structural formulas of three SCAs containing amino (APTES), phenylamino (TMSPA), and sulfhydryl (MPTMS) groups (Figure S1). APTES, featuring an aromatic amine ($-NH_2$) terminus, was chosen as a benchmark flexible, amine-terminated coupler. Its primary role is to establish covalent bonds with the epoxy matrix. TMSPA, featuring an aromatic amine (-NH-Ph) terminus, was selected to probe the effect of molecular rigidity and π–π conjugation. MPTMS, featuring a thiol (-SH) terminus, was specifically selected to investigate the influence of heterogeneous atoms in the terminal group. The three different SCAs could provide a critical comparison for understanding how

16163028, 0, Downloaded from https://advanced.onlinelibrary.wiley.com/doi/10.1002/adfm.202522804 by Zhejiang University, Wiley Online Library on [07/04/2026]. See the Terms and Conditions (https://onlinelibrary.wiley.com/terms-and-conditions) on Wiley Online Library for rules of use; OA articles are governed by the applicable Creative Commons License

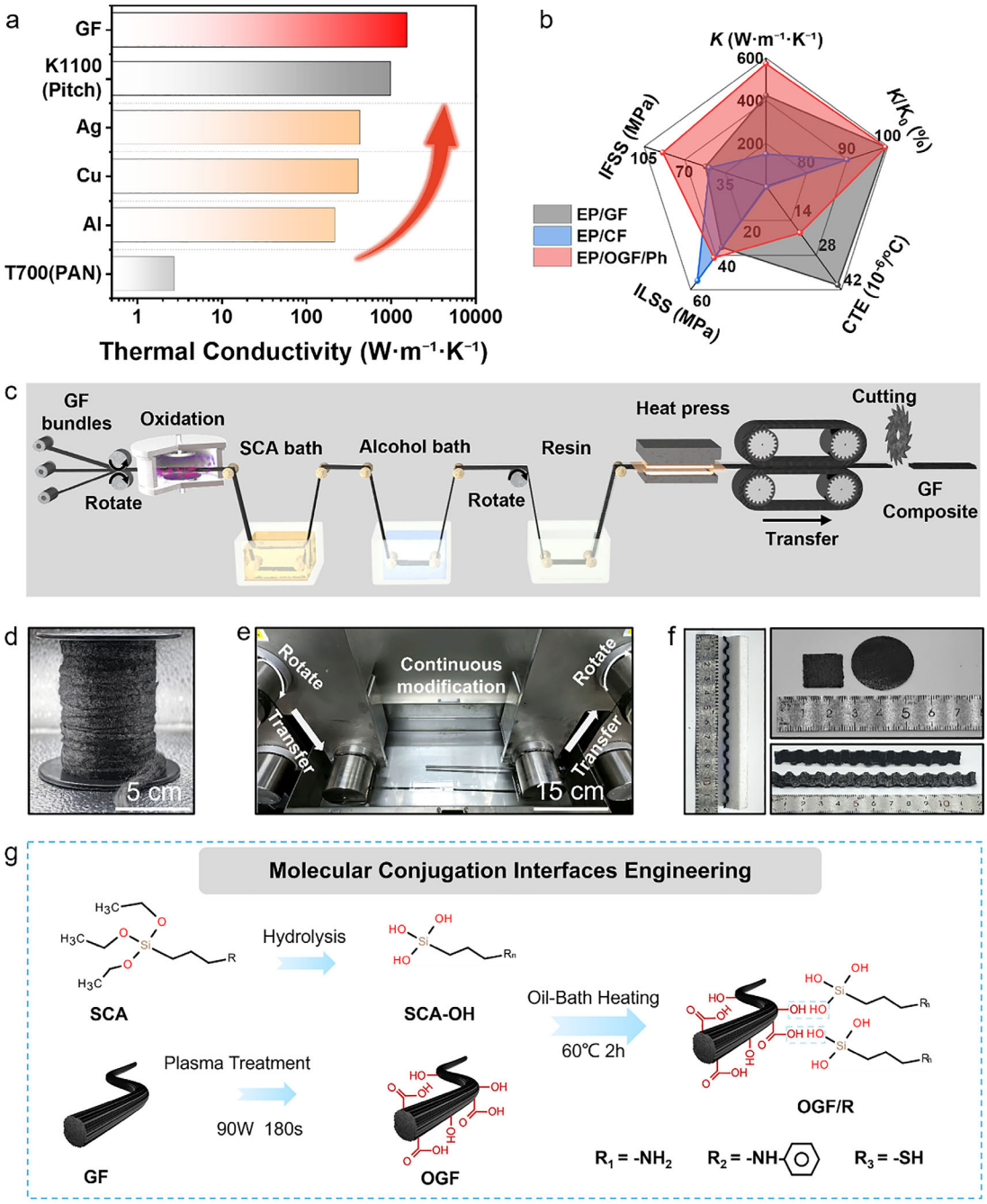

FIGURE 1 | (a) Comparison of the thermal conductivity of GF filaments and other traditional thermal conduction materials, including K1100 (Pitch-based CF), silver, copper, aluminum and T700 (PAN-based CF). (b) Comparison of the IFSS, ILSS, in-plane thermal conductivity (K), retention rate (K/K_0) and thermal expansion of EP/GF, EP/OGF/Ph, and EP/CF. (c) Schematic diagram of large-scale continuous preparation of GF composites. (d–f) Photograph of GF bundle (d), SCA bath (e) and GF composites (f). (g) Molecular conjugation interface engineering for highly thermally conductive and high strength GF composites.

this fundamental property affects interfacial mechanical and thermal transport.

Initially, the aligned GF bundles underwent plasma treatment to introduce oxygen-containing functional groups (denoted as OGF), facilitating subsequent SCA modification. As shown in Figure 2a, the untreated GFs exhibited rough surfaces with hierarchical wrinkles along the longitudinal direction. After plasma etching for 180s, the OGFs showed further enhanced roughness (Figure S3), which not only improved the mechanical interlocking between the GFs and EP, but also provided a larger surface area for SCA adhesion. Energy-dispersive spectroscopy (EDS) mapping confirmed that OGFs exhibited a significant increase in oxygen content compared to the trace oxygen on the pristine GFs.

Subsequently, the OGFs were individually immersed in three typical SCA solutions to construct molecular selective interphase

16163028, 0, Downloaded from https://advanced.onlinelibrary.wiley.com/doi/10.1002/adfm.202522804 by Zhejiang University, Wiley Online Library on [07/04/2026]. See the Terms and Conditions (https://onlinelibrary.wiley.com/terms-and-conditions) on Wiley Online Library for rules of use; OA articles are governed by the applicable Creative Commons License

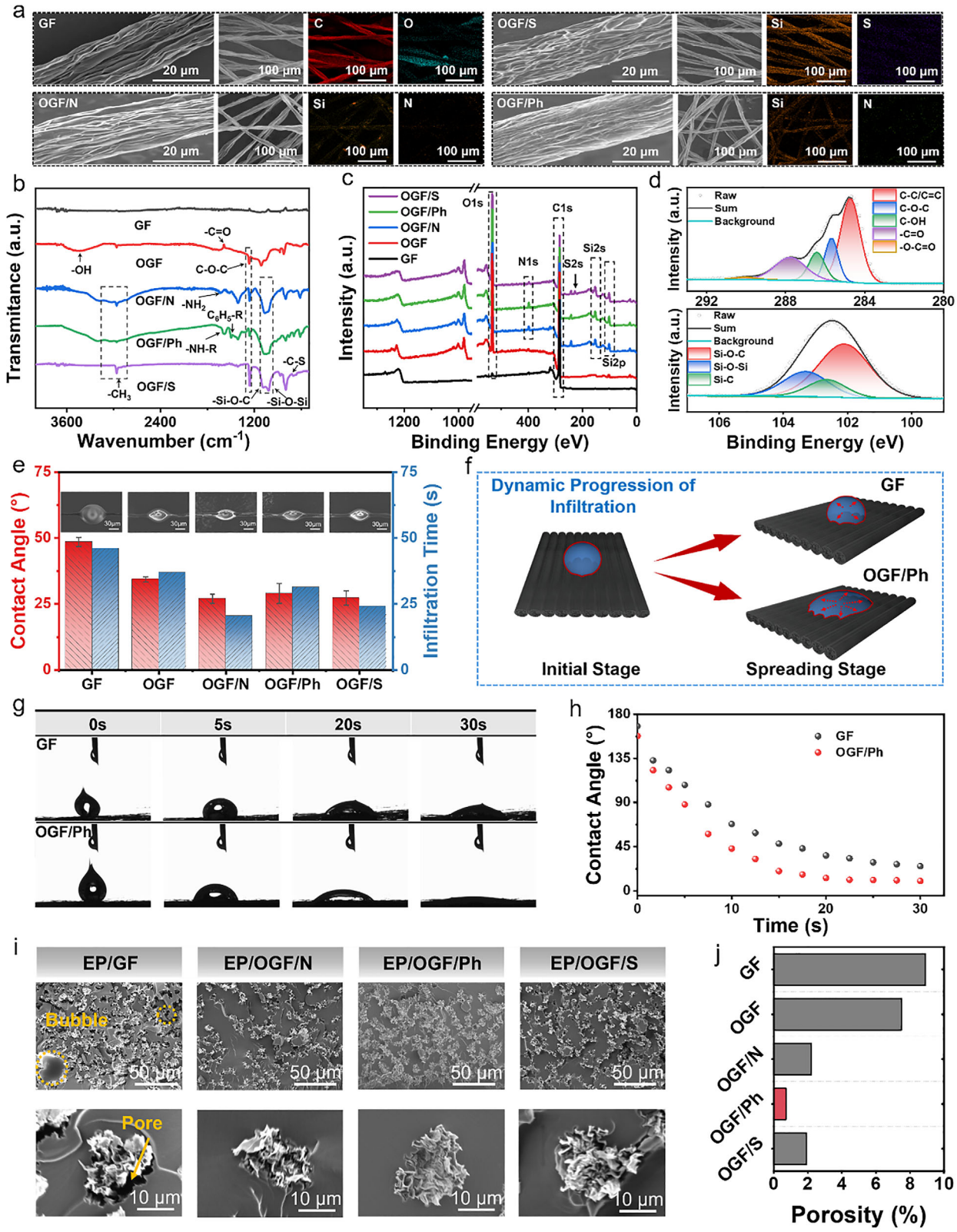

FIGURE 2 | (a) SEM and EDS image of GF, OGF/N, OGF/Ph and OGF/S. (b,c) The FTIR spectrum (b) and the XPS wide-scan spectrum (c) of GF, OGF/N, OGF/Ph and OGF/S. (d) High-resolution C1s spectrum of OGF and Si2p of OGF/Ph. (e) Contact angle of EP to GF and infiltration time of EP on GF bundles. (f,g) Schematic diagram (f) and photograph (g) of the EP spreading process at GF and OGF/Ph bundles. (h) Temporal evolution of resin contact angle on GF bundles. (i) Cross-sectional images of EP/GF, EP/OGF/N, EP/OGF/Ph and EP/OGF/S. (j) Comparison of the porosity of EP/GF, EP/OGF/N, EP/OGF/Ph and EP/OGF/S.

16163028, 0, Downloaded from https://advanced.onlinelibrary.wiley.com/doi/10.1002/adfm.202522804 by Zhejiang University, Wiley Online Library on [07/04/2026]. See the Terms and Conditions (https://onlinelibrary.wiley.com/terms-and-conditions) on Wiley Online Library for rules of use; OA articles are governed by the applicable Creative Commons License

on the GFs surface functionalized with amino, phenylamino and sulfhydryl groups, yielding SCA-functionalized GFs named as OGF/N, OGF/Ph, and OGF/S, respectively. Rigorous ethanol rinsing was conducted to eliminate unreacted SCAs and byproducts, ensuring contaminant-free interfaces. After grafting with SCAs, SEM observations suggested that the surface wrinkles became shallower. This morphological change was quantitatively confirmed by surface roughness measurements (Figure 2a; Figures S4 and S5), which showed a reduction in the arithmetic mean height (Sa) from 1.89 μm (OGF) to 0.90–1.04 μm. The formation of a siloxane interphase is responsible for this smoothing effect and confirms the successful SCA modification. The EDS further revealed uniform distribution of Si and characteristic elements (N, S) on GF surface, validating stable and effective SCA modification of hierarchical wrinkle topologies [44].

As shown in Figure 2b, the Fourier-transform infrared spectra (FTIR) provides insight into the chemical functional groups of GFs. Compared with the untreated GFs, the OGFs exhibited a broad -OH stretching peak at 3430 cm^{-1}, carbonyl (-C = O) stretching peak at 1675 cm^{-1}, and asymmetric ether bond (-C-O-C-) stretching at 1260 cm^{-1} [45]. When grafted with APTES, the OGF/N displayed overlapping -NH_2 stretching and -CH_3 symmetric/asymmetric vibrations at 3000–3500 cm^{-1}, and -NH_2 in-plane bending at 1630 cm^{-1} [46]. Similarly, OGF/Ph exhibited secondary amine (-NH-) vibration at 1580 cm^{-1}, accompanied by mono-substituted benzene ring (-C_6H_5) bending at 1492 cm^{-1} [47]. For MPTMS-modified OGF/S, while the -SH bond signal was weak, the distinct C—S bond stretching was confirmed at 665 cm^{-1} [48]. All SCA-treated GFs exhibited the Si-O-C (1085 cm^{-1}) and Si-O-Si (1019 cm^{-1}) stretching vibrations, verifying the dehydration condensation reaction between the SCAs and oxidized GFs (Si-O-C) and polysiloxane chain formation through silane hydrolysis and intermolecular condensation (Si-O-Si). Collectively, these spectral signatures demonstrate successful SCA grafting onto GF surfaces [49].

To further investigate the evolution of chemical elements and functional groups on the surface of GFs before and after SCAs modification, X-ray photoelectron spectroscopy (XPS) analysis was conducted. The elemental composition and functional group variations are presented in Figure 2c, and detailed quantitative comparisons of the surface characteristics are provided in Table S1. After oxidation, the surface oxygen content of OGFs reached 26.2 at.% and the C1s high-resolution spectrum of OGFs was divided into C-C/C = C (~284.8 eV), C-O-C (~285.6 eV), C-OH (~286.6 eV), C = O (~287.8 eV), and HO-C = O (~289.3 eV) peaks (Figure 2d; Figure S6a) [50]. Furthermore, the Si2p peak appeared in the wide-angle scanning spectra of OGF/N, OGF/Ph and OGF/S. The measured silicon contents were 3.0 at.%, 3.6 at.%, and 3.6 at.%, respectively (Table S1) [51]. As shown in Figure 2d and Figure S6b, the high-resolution Si2p spectrum revealed Si-O-C (~102.2 eV), Si-C (~102.6 eV), and Si-O-Si (~103.4 eV) peaks. Notably, while the SCA-treated GFs exhibited comparable silicon content, the GF/S demonstrated a higher Si-O-Si/Si-O-C ratio (59.5%) than OGF/N (33.3%) and OGF/Ph (38.5%) (Table S2). This disparity suggests a preferential self-reaction of MPTMS during hydrolysis. This self-reaction consumes excessive hydroxyl groups through siloxane bond formation, thereby impairing the ability of SCA to interact effectively with the OGFs.

Superior wettability facilitates more intimate contact between the fibers and the EP during curing, which is crucial for achieving the desired interfacial morphology. The static contact angle of the pristine GF with the EP was measured to be 48.5°, decreasing to 34.4° after plasma treatment. Notably, compared to the pristine GF, the OGF/N, OGF/Ph, and OGF/S exhibited further significant reductions, with contact angles of 27.0°, 29.0°and 26.3°, decreased by 44.3%, 40.2%, and 45.8%, respectively. In addition, the dynamic wetting behavior during EP infiltration quantitatively demonstrates the interfacial modification efficacy. It took 46.1 s for unmodified GFs bundles to achieve nearly complete resin permeation, which is objectively defined as the time when the dynamic contact angle decreases closely to 0° accompanied by a virtually flat meniscus profile, while plasma treating reduced this duration to 37.0 s. SCA-treated GFs with different molecular tethers agents exhibited further kinetic acceleration with 20.4 s (OGF/N), 31.2 s (OGF/Ph) and 24.0 s (OGF/S), respectively (Figure 2e). To gain deeper insight into the underlying mechanism, the evolution of dynamic contact angles over time was monitored. The untreated GF and silane-modified GF (taking OGF/Ph as an example) exhibited initial wetting angles of 159.5° and 149.2°, respectively. After 30s, the unmodified GF's contact angle decreased to 22.5°. By contrast, OGF/Ph exhibited superior wetting, reaching only 8.3° within the same time, which is attributed to the enhanced compatibility conferred by the phenylamino functionality (Figure 2g,h). Compared with pristine GFs, OGF/Ph showed faster reduction in contact angle, promoting rapid EP propagation along fiber axes and inter-fiber channels (Figure 2f). Thus, the molecular conjugation-tailored surfaces fundamentally lower interfacial energy barriers, as quantitatively evidenced by the increased surface free energy, from 23.6 mN m^{-1} for pristine GF to 30.3 mN m^{-1} for OGF/Ph (Figure S7), enabling near-spontaneous resin infiltration for GFs.

GF composites were engineered through the vacuum-assisted resin infusion process, and the related composites are categorized as EP/GF, EP/OGF, EP/OGF/N, EP/OGF/Ph, and EP/OGF/S. As shown in Figure 2i, the cross-sections of the GF composites are revealed two dominant defect types. Two distinct types of defects are identified: fiber-adjacent pores due to incomplete EP penetration into micro-wrinkles from poor wettability, whereas curing-induced bubbles form from the aggregation of voids driven by EP shrinkage. Quantitative analysis using ImageJ software demonstrated dramatic porosity reduction through molecular conjunction interfaces engineering (Figure S8). The reported values represent the average of at least three independent samples per group [52, 53]. The EP/GF exhibited a porosity of 8.9%, decreasing to 7.5% for EP/OGF. The use of SCA-modified GFs further led to remarkably reduced porosities: 1.9% for EP/OGF/N, 0.77% for EP/OGF/Ph, and 2.2% for EP/OGF/S (Figure 2j). The champion EP/OGF/Ph shows phenylamino-group enhanced interfacial compatibility, effectively eliminating both wetting-related voids and curing defects through optimized resin-fiber interaction.

2.2 | Interface Bonding and Failure Mechanism of GF Composites

The IFSS serves as a core indicator for evaluate the interfacial performance of composites. As illustrated in Figure 3a, the IFSS

16163028, 0, Downloaded from https://advanced.onlinelibrary.wiley.com/doi/10.1002/adfm.202522804 by Zhejiang University, Wiley Online Library on [07/04/2026]. See the Terms and Conditions (https://onlinelibrary.wiley.com/terms-and-conditions) on Wiley Online Library for rules of use; OA articles are governed by the applicable Creative Commons License

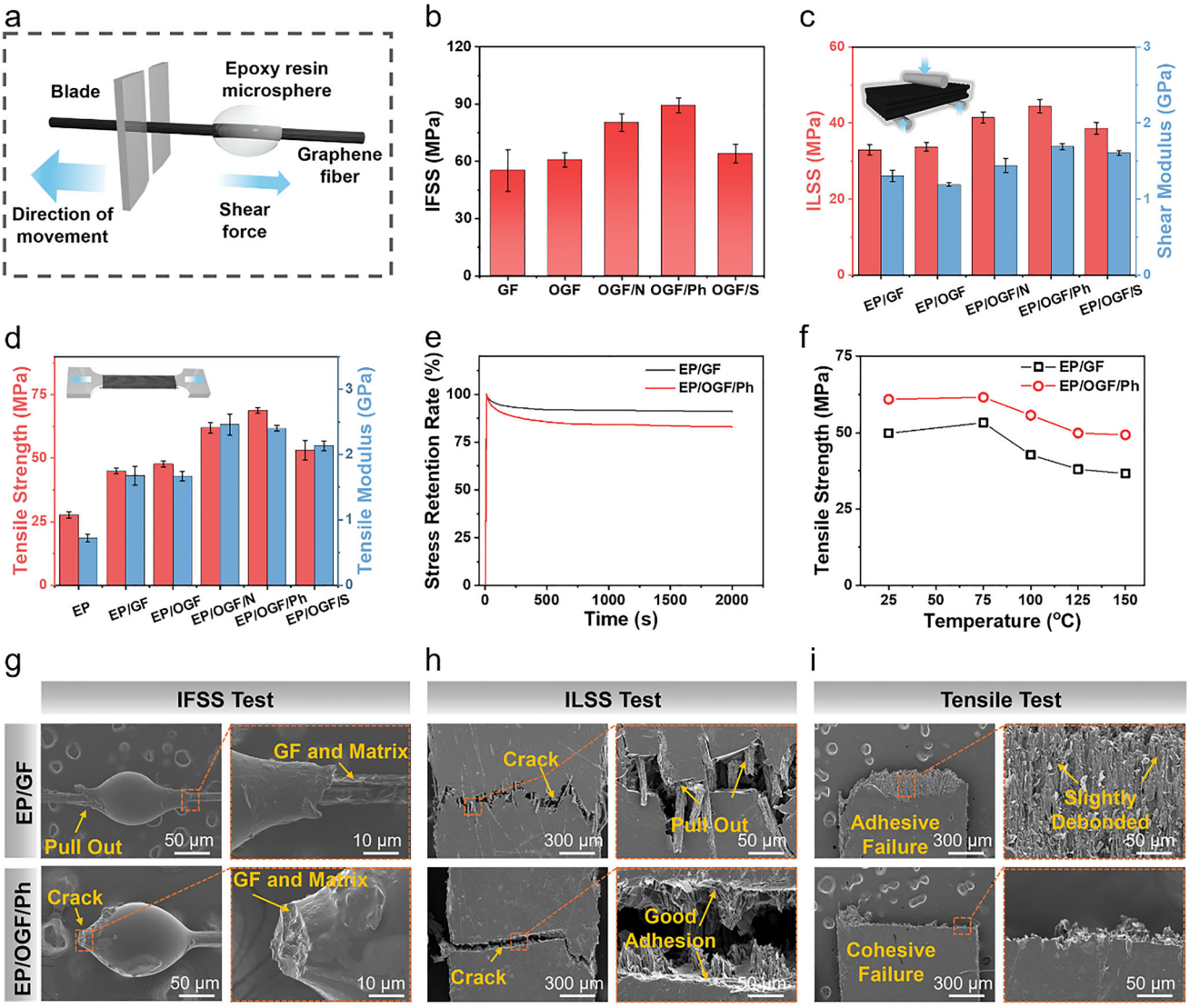

FIGURE 3 | (a) Schematic diagram of IFSS test. (b–d) IFSS (b), ILSS (c) and tensile strength (d) of the EP/GF, EP/OGF, EP/OGF/N, EP/OGF/Ph and EP/OGF/S. (e,f) Stress relaxation (e) and thermal aging tests (f) for EP/GF and EP/OGF/Ph. (g–i) SEM images of fractured surface after IFSS (g), ILSS tests (h) and tensile strength (i).

measurements are conducted via single-fiber pull-out testing to quantitatively demonstrate enhanced interfacial bonding in modified GF composites. The baseline EP/GF exhibited an IFSS of only 55.2 MPa, while the IFSS of EP/OGF increased to 60.8 MPa (Figure 3b; Figure S9). This enhancement primarily originates from enhanced mechanical interlocking and the hydrogen bonding via introducing oxygen-containing groups [54]. The customizing molecular conjugation interphase design dramatically elevated the interface interactions. Specifically, the IFSS of OGF/N, OGF/Ph and OGF/S reached 80.3, 89.2, and 64.1 MPa, with increment of 45.5%, 61.6%, and 16.0%, respectively. Notably, the IFSS of OGF/N and OGF/Ph surpassed conventional CF composites (40–80 MPa, Table S3). This significant enhancement of interfacial mechanical properties is attributed to the synergistic mechanism between the dual molecular-scale mechanism and the reduction of interface porosity. Specifically, the surface modification of GFs through molecular conjugation interface engineering has greatly enhanced the wettability between resins, significantly reducing the formation of interfacial pore defects. This lays an excellent structural foundation for improving the interfacial strength. Meanwhile, the SCA molecules further enhance the interfacial interaction between GFs and resins through dual molecular-scale mechanisms to promote the transfer of mechanical loads and interfacial reinforcement. The flexible silane polymer layer on the fiber surface enabled chain entanglement with EP and the -NH_2, -NH-Ph and -SH terminal functional groups participated in EP ring-opening reactions during curing to form covalent bonds [55–57]. Besides, the presence of the benzene ring in OGF/Ph establishes additional π-π interactions with the aromatic components of EP at the interfaces to strengthen the interfacial interaction. Thus, the molecular conjugation interface engineering effectively reduces the interfacial defects and improves the interfacial interactions to boost the final interfacial mechanical properties of GF composites.

To evaluate how the enhanced interfaces shear strength improves the mechanical performance of the composites, we systematically

16163028, 0, Downloaded from https://advanced.onlinelibrary.wiley.com/doi/10.1002/adfm.202522804 by Zhejiang University, Wiley Online Library on [07/04/2026]. See the Terms and Conditions (https://onlinelibrary.wiley.com/terms-and-conditions) on Wiley Online Library for rules of use; OA articles are governed by the applicable Creative Commons License

investigated the effects of plasma treatment and SCA modification on interfacial characteristics through interlaminar shear strength (ILSS) and tensile strength measurements. The corresponding results are presented in Figure 3c,d and Figures S10 and S11. At 20% fiber volume fraction, the ILSS of untreated EP/GF composites was 32.9 MPa. Plasma-treated EP/OGF composites showed negligible change, with the ILSS remaining at 33.8 MPa. By contrast, coupling agent-modified composites demonstrated significant enhancements: EP/OGF/N achieved 41.5 MPa (25.9% increase), EP/OGF/Ph reached 44.4 MPa (34.9% increase), and EP/OGF/S attained 38.6 MPa (17.0% increase). Similarly, the tensile strength increased marginally from 44.9 MPa of EP/GF to 47.7 MPa of EP/OGF. By contrast, SCA modification substantially improved the performance, with EP/OGF/Ph demonstrating the highest tensile strength of 68.8 MPa, corresponding to a 53.1% enhancement compared to EP/GF. Other modified systems exhibited intermediate improvements: EP/OGF/N reached 62.0 MPa (38.1% increase) and EP/OGF/S attained 53.1 MPa (18.3% increase).

The structural stability evaluated by stress relaxation and thermal aging tests under extreme thermomechanical conditions is critical for practical applications. The interfaces-engineered EP/OGF/Ph composites exhibited superior resistance. Specifically, stress relaxation tests conducted at room temperature under 2% strain for 2000 s revealed retention rates of 83.1% for EP/GF and 91.0% for EP/OGF/Ph compared to their initial values (Figure 3e). The relaxation kinetics identified two distinct stages: an initial rapid stress decay (0–750 s) attributed to concurrent molecular chain disentanglement and interfacial micro-slip. Subsequent linear relaxation (750–2000 s) showed minimal stress reduction, indicating stabilized network structure. 6 h thermal aging tests were conducted at different temperatures (Figure 3f). Both composites exhibited slight strength enhancement peaking at 75°C (7.1% increase of EP/GF and 1.1% increase of EP/OGF/Ph), correlating with the curing reaction and molecular rearrangement activation. Severe degradation occurred at 150°C, with residual strengths reduced to 73.5% (EP/GF) and 81.0% (EP/OGF/Ph). This deterioration stemmed from resin decomposition-induced microcracks and thermal expansion mismatch-induced interfacial delamination at fiber/matrix interfaces, which could be confirmed by the thermogravimetric curve (Figure S12) and the subsequent study on the thermal expansion coefficient (TEC). The covalent bonding network of EP/OGF/Ph could substantially mitigate damage propagation compared to physically anchored structure of EP/GF.

Fracture morphology analysis following IFSS tests reveal fundamental differences in failure mechanisms between EP/GF and EP/OGF/Ph composites (Figure 3g). The EP/GF exhibits characteristic pull-out failure zones, indicating a weak interfacial bonding. The fracture was initiated at the fiber-matrix interface due to stress concentration, with the failure mechanism being predominantly governed by adhesive failure. The slight EP residues observed on the fiber surface further indicate inadequate interfacial adhesion strength. By contrast, EP/OGF/Ph exhibited cohesive failure with rich EP residue, indicating the strong interfacial bonding strength. This transition from adhesive failure to cohesive failure confirms the effectiveness of molecular conjugation interface engineering design.

Complementary ILSS fracture analysis further verifies the fracture mechanism shift (Figure 3h). The EP/GF exhibited obvious fibers pullout (>80 μm displacement) with negligible EP residue on the extracted fibers, indicating weak interfacial bonding that was primarily based on physical interlocking. The EP/OGF/Ph exhibited shortened pull-out lengths (<30 μm) and substantial matrix fragments adherent to fibers. The tensile fracture plane morphology provides additional validation that the fracture profile of EP/GF signifies interfacial delamination with insufficient bonding strength between composite layers (Figure 3i). By contrast, the fracture surface of EP/OGF/Ph, characterized by zigzag matrix crack paths, fiber fracture, and matrix cracking, demonstrated optimized stress transfer. The zigzag crack propagation path in modified EP/OGF/Ph composites showed that the molecularly engineered bonding interfaces enhance fracture energy dissipation, enabling effective crack deflection at interfaces.

2.3 | Thermal Properties of GF Composites

Superior interfacial bonding in GF composites directly enhances the in-plane thermal conductivity by minimizing phonon scattering defects and constructing efficient phonon transmission interfaces [58]. Unless otherwise specified, the thermal conductivities reported in the manuscript are all the in-plane thermal conductivities (along the fiber axis direction). The EP/OGF/Ph achieved an in-plane thermal conductivity of 571.1 W m^{-1} K^{-1} at 60 vol% fiber loading, representing a 34.6% increase over the unmodified EP/GF (424.4 W m^{-1} K^{-1}) and exceeding that of most CF composites (Figure 4a; Figure S15 and Table S4). In addition, the in-plane thermal conductivities of EP/OGF, EP/OGF/N, and EP/OGF/S were 455.6, 503.1, and 477.2 W m^{-1} K^{-1} (Table S5), respectively. The in-plane thermal conductivity demonstrated nonlinear scaling with fiber content, showing slowed enhancement rates beyond 50 vol%. This phenomenon is attributed to both microstructural defects and saturation effect in thermal conduction pathways. SEM observations (Figure S16a,b) confirm that high-pressure processing at elevated filler loadings (e.g., 60 vol%) induces two critical issues: fiber fracture, which severs continuous thermal pathways, and inadequate epoxy resin impregnation. These issues collectively result in interfacial voids that severely disrupt phonon transport. Concurrently, beyond a critical fiber density, the formation of new efficient thermal pathways diminishes (Figure S16c). Consequently, it leads to a decrease in the thermal conductivity growth of the GF composite under high filling content. Furthermore, after 100 thermal cycles (25 to 125°C), both EP/GF and EP/OGF/Ph at 60 vol% fiber loading maintained excellent thermal conductivity retention above 98% (Figure 4b; Figure S19). Separately, to evaluate long-term environmental stability, hygrothermal aging tests (75°C/75% RH for 14 days) were conducted. Both EP/GF and EP/OGF/Ph composites demonstrated excellent and comprehensive stability. Specifically, they retained over 88% of their original tensile strength and over 97% of their in-plane thermal conductivity after aging (Figure S18), which collectively confirms their robust structure stability.

Thermal expansion measurements were conducted on EP and GF composites, with particular attention paid to their anisotropic thermal expansion characteristics in the longitudinal and

16163028, 0, Downloaded from https://advanced.onlinelibrary.wiley.com/doi/10.1002/adfm.202522804 by Zhejiang University, Wiley Online Library on [07/04/2026]. See the Terms and Conditions (https://onlinelibrary.wiley.com/terms-and-conditions) on Wiley Online Library for rules of use; OA articles are governed by the applicable Creative Commons License

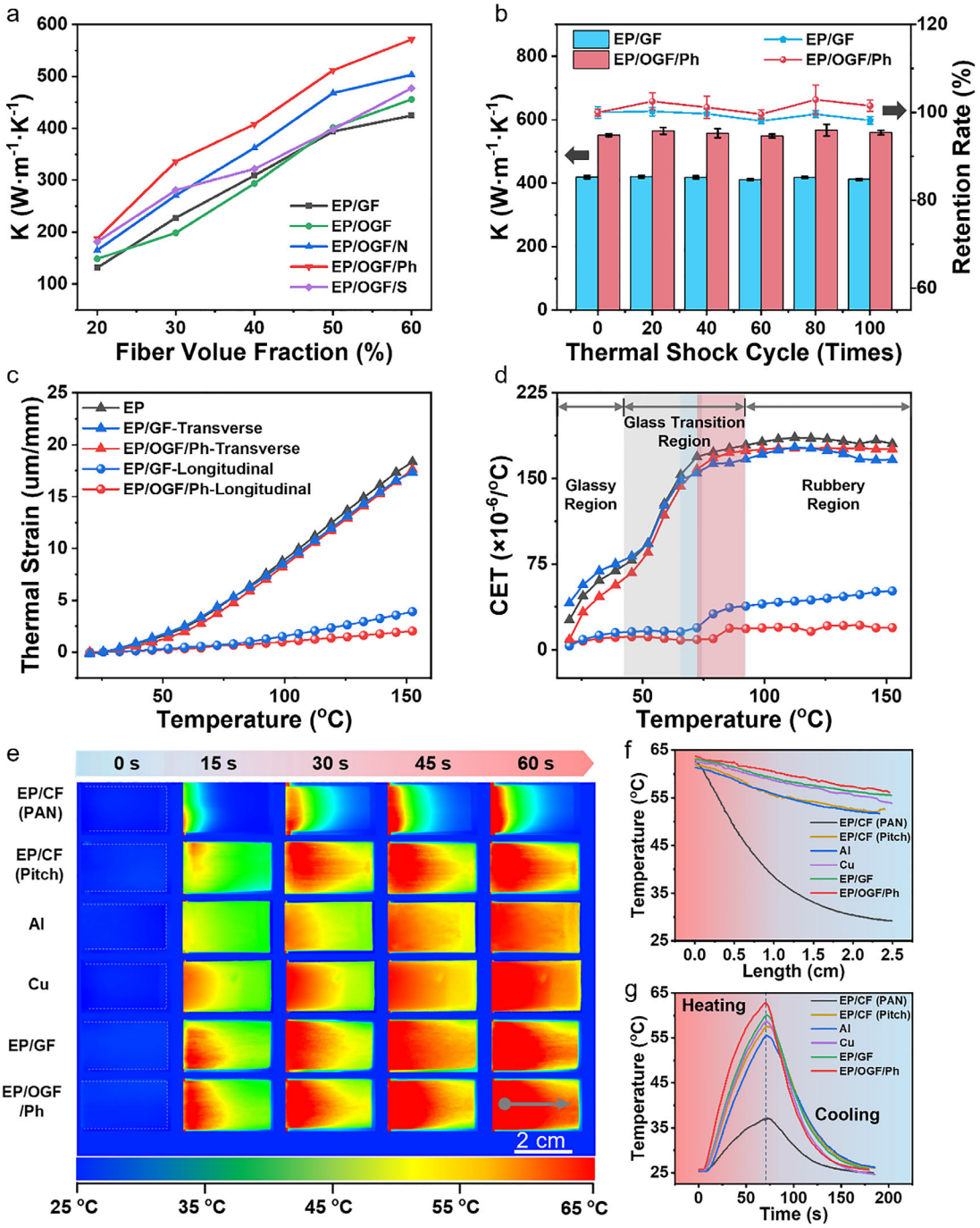

FIGURE 4 | (a) In-plane thermal conductivity (K) of EP/GF, EP/OGF, EP/OGF/N, EP/OGF/Ph and EP/OGF/S. (b) The thermal conduction retention (K/K_0) of EP/GF and EP/OGF/Ph under cyclic heating loading from 25 to 125°C. (c,d) Thermal strains (c) and linear CTE (d) of EP, EP/GF, EP/OGF, EP/OGF/N, EP/OGF/Ph in transverse and longitudinal direction. (e) IR photographs of different samples. (f) Axial temperature distribution of thermal gradient evolution. (g) Temporal temperature evolution in thermal shock condition.

transverse orientations [59]. The testing protocol employed a heating rate of 5°C min^{-1} across the temperature range of 25–150 °C under nitrogen atmosphere. As shown in Figure 4c,d, pure EP exhibited a thermal strain of 18.63×10^{-3} with a corresponding coefficient of thermal expansion (CTE) of 139.5 $\times 10^{-6}$/°C. In the longitudinal direction, both EP/GF(∥) and EP/OGF/Ph(∥) demonstrated significantly constrained thermal deformation, with strains reduced to 3.91×10^{-3} and 2.04×10^{-3}, respectively. This corresponded to CTE values of 40.02×10^{-6}/°C and 19.08×10^{-6}/°C, representing a remarkable 52.3% reduction in CTE for EP/OGF/Ph(∥). Conversely, in the transverse direction, thermal strain reached 17.34×10^{-3} (EP/GF(⊥)) and 17.62×10^{-3} (EP/OGF/Ph(⊥)), with CTEs of 131.5 $\times 10^{-6}$/°C and 133.1 $\times 10^{-6}$/°C, respectively. This pronounced anisotropy is directly evidenced by dynamic mechanical analysis (DMA). As shown in Figure S20, the room-temperature storage modulus (E') was significantly higher in the longitudinal direction than in the transverse direction. For instance, the value for EP/OGF/Ph(∥)

16163028, 0, Downloaded from https://advanced.onlinelibrary.wiley.com/doi/10.1002/adfm.202522804 by Zhejiang University, Wiley Online Library on [07/04/2026]. See the Terms and Conditions (https://onlinelibrary.wiley.com/terms-and-conditions) on Wiley Online Library for rules of use; OA articles are governed by the applicable Creative Commons License

was 12.2 GPa, compared to 4.9 GPa for EP/OGF/Ph(⊥). Concurrently, the peak loss factor (tgδ) was drastically lower longitudinally (0.18) than in the transverse direction (0.73). These DMA results robustly demonstrate a highly constrained and rigid architecture along the fiber direction, originating from the stark difference in molecular chain confinement and interfacial constraint. The incorporation of GF significantly altered the glass transition behavior of pure EP, as verified by the tangent method to determine the glass transition point of GF composites. This measurement quantified the transition point at which the CTE exhibits a characteristic discontinuity during controlled heating. Pure EP exhibited a broad glass transition range of 46–79 °C, whereas the EP/GF showed an elevated transition region of 66–92 °C. Molecular conjugation interface engineering in EP/OGF/Ph further enhanced the transition profile to 73–92 °C, elevating the onset temperature by 27°C compared to pure EP. Notably, the glass transition range derived from thermal expansion tests align well with those obtained from DMA. These shifts arose from synergistic interactions of two mechanisms: the physical confinement of polymer chains within the fiber network and covalent bonding between polymer molecules and phenyl/imino groups. Physical confinement reduces free volume mobility, while covalent bonding enhances interfacial stress transfer efficiency.

To quantitatively benchmark the application potential of GF composites for thermal management, the heat dissipation capabilities of EP/GF, EP/OGF/Ph, copper, aluminum, and CF composites (PAN-/Pitch-based) were compared along the axial direction under identical heating power (Figure 4e; Figure S21). The results revealed that EP/OGF/Ph achieved a temperature reduction of 7.5°C (from 63.7 to 56.2°C), outperforming all counterparts (Figure 4f). Importantly, EP/OGF/Ph exhibits metal-level thermal management capability, outperforming both aluminum and the copper in heat dissipation. Beyond steady-state performance, the dynamic thermal regulation capability was further evaluated under thermal shock condition. Remarkably, during thermal shock tests, EP/OGF/Ph demonstrated superior thermal regulation capabilities (Figure 4g). It achieved the highest heating and cooling rates of 38.2 and 25.4°C min^{-1}, respectively, surpassing those (33.1 and 22.1°C min^{-1}) of EP/GF. This accelerated thermal response allowed EP/OGF/Ph to reach a maximum temperature of 63.2°C after 60 s of heating, which is significantly higher than that (58.1°C) of EP/GF and maintaining faster heat dissipation during the cooling phase. In summary, GF composites enable transformative thermal management solutions by leveraging graphene's intrinsically high thermal conductivity and establishing multiscale phonon transport channels through molecularly engineered covalent interfaces. Consequently, this approach achieves unprecedented interfacial strength and heat dissipation efficiency while maintaining structural stability under extreme thermal gradients, enabled by synergistic defect suppression and phonon scattering minimization.

2.4 | Molecular Dynamics of Interfacial Heat Transport

As illustrated in Figure 5a,b and Figures S22 and S24, non-equilibrium molecular dynamics (NEMD) simulations were further conducted to elucidate the enhanced ITC in molecular conjugation interface-engineered GF composites, including interfaces grafted with APTES, MPTMS, and TMSPA. The silane molecule grafting sites were uniformly distributed on the graphene surface with grafting density of ~ 2.8 molecules nm^{-2} (Figure S25a). Two atomic-level configurations were constructed with silane agents either solely chemisorbed onto the graphene surface or further covalently linked to the crosslinked EP matrix. Prior to quantitative analysis, convergence tests were performed on the graphene cross-sectional area, number of layers, and simulation time to ensure the stability and size-independence of the obtained ITC values (Figure S23). As shown in Figure 5c, grafting TMSPA onto graphene significantly increased the ITC from 54.03 ± 5.72 MW m^{-2} K^{-1} (unmodified interface) to 143.83 ± 14.40 MW m^{-2} K^{-1} through enhanced phonon coupling. Further extension of the TMSPA network into the polymer matrix led to a substantial rise to 373.56 ± 8.13 MW m^{-2} K^{-1}. Such a 7 times enhancement in ITC was attributable to phenyl-conjugation induced phonon coupling and cross-linked network continuity.

Preliminary molecular structure analysis reveals that the ITC enhancement is governed by coupling agent groups and molecular rigidity (Figure 5d–f; Figure S25b). APTES modified with a small, non-planar primary amine (NH_2) exhibits rotational freedom that randomizes C—N bond orientations, yielding a disordered interface that hampers phonon transmission. MPTMS ends with a thiol (SH) reacts with EP to form C—S bonds. However, these bonds are longer and weaker than their C—N counterparts, leading to looser interfacial contacts and suboptimal ITC. By contrast, the rigid aromatic amine structure of TMSPA enables planar benzene ring alignment with the EP network, forming strong directional C—N bonds [60]. The molecular constraint suppresses rotational freedom and promotes an ordered conjugation interfacial configuration, substantially boosting phonon coupling efficiency for superior ITC. The direct correlation between molecular rigidity, interfacial order, and thermal transport efficiency provides foundational molecular conjugation interface design principles for advanced thermally conductive GF composites.

2.5 | Conductance Mechanism Mechanistic Analysis of ITC

To elucidate the ITC enhancement mechanism, we analyzed the vibrational density of states (VDOS) derived from velocity autocorrelation functions (VACF) with confirmed convergence (Figure 5g–i; Figures S26 and S27). Graphene exhibits dominant phonon modes within the low-frequency window of 0–40 THz, while the EP matrix possesses a broader spectrum peaking at 20–50 THz with a distinct high-frequency band at 85–95 THz. Despite some overlap in the mid- to low-frequency region, the two components exhibit substantial phonon spectral misalignment. Crucially, within the principal 0–40 THz band of graphene, EP shows near-zero spectral density contribution. The phonon mismatch is the primary origin of intrinsic ITC limitations in unmodified interface, particularly with the 40–85 THz spectral gap.

Grafting the coupling agents introduces additional vibrational modes with the mid-frequency band, effectively enhancing the

16163028, 0, Downloaded from https://advanced.onlinelibrary.wiley.com/doi/10.1002/adfm.202522804 by Zhejiang University, Wiley Online Library on [07/04/2026]. See the Terms and Conditions (https://onlinelibrary.wiley.com/terms-and-conditions) on Wiley Online Library for rules of use; OA articles are governed by the applicable Creative Commons License

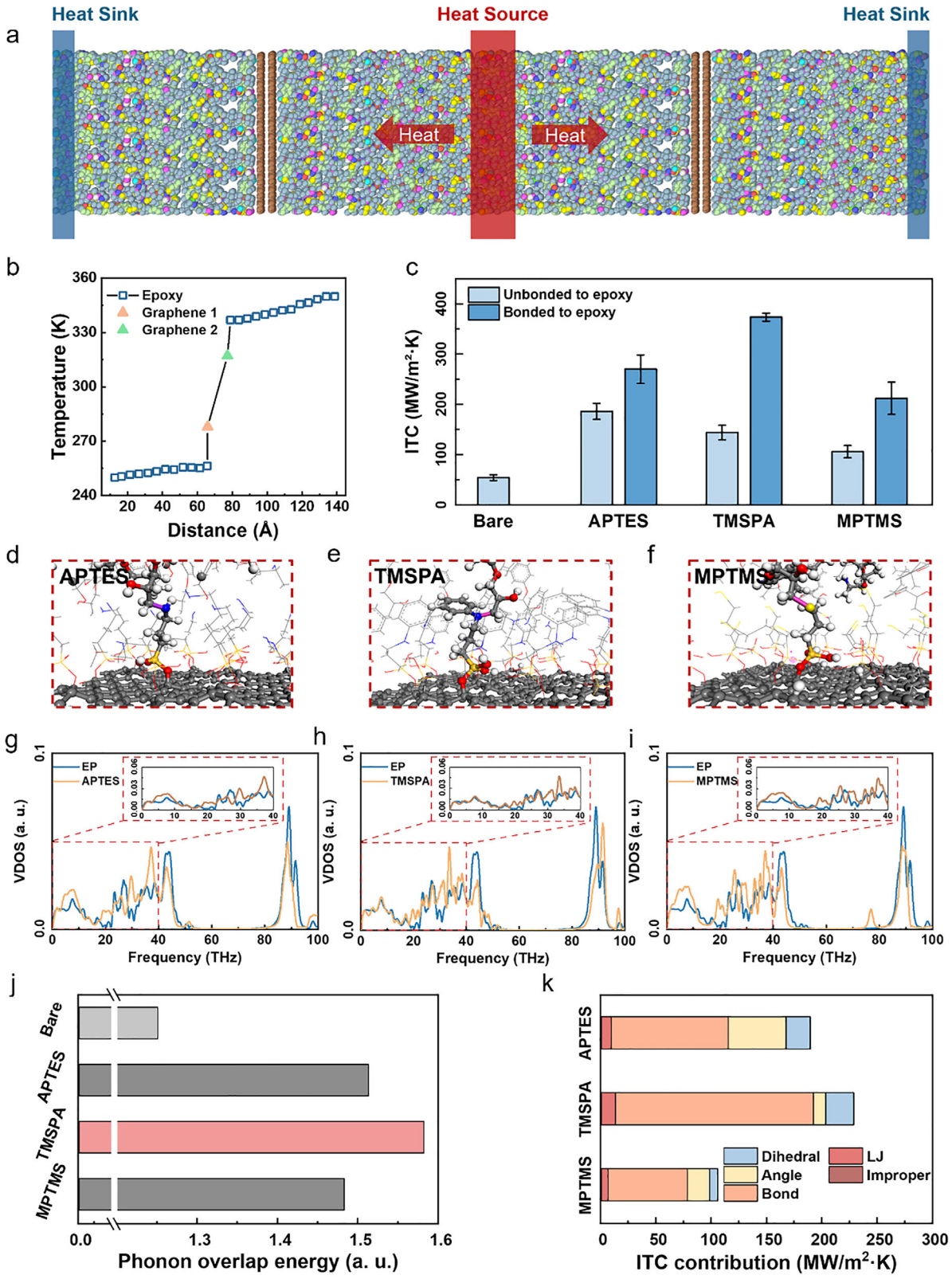

FIGURE 5 | (a) EP/graphene layered stacking model. (b) Temperature gradient at the interface. (c) ITC of different coupling agents under grafting-only and grafting-with-crosslinking conditions. (d–f) Schematic diagram of APTES (d), TMSPA (e) and MPTMS (f) grafted molecules. (g–i) Comparison of the VDOS of EP with APTES (g), TMSPA (h) and MPTMS (i). (j,k) Phonon overlap energy (j) and decomposition of heat flux (k) between different coupling agents and EP.

16163028, 0, Downloaded from https://advanced.onlinelibrary.wiley.com/doi/10.1002/adfm.202522804 by Zhejiang University, Wiley Online Library on [07/04/2026]. See the Terms and Conditions (https://onlinelibrary.wiley.com/terms-and-conditions) on Wiley Online Library for rules of use; OA articles are governed by the applicable Creative Commons License

graphene-EP overlap and establishing an effective phonon bridge. Apart from providing covalent bonding across the interface, this molecular conjugation interface engineering achieves critical phonon spectrum alignment in the 0–40 THz window, where enhanced VDOS closely matches the low-frequency phonons of EP. In particular, the TMSPA-modified interface demonstrates notable frequency alignment, with modes at 8 and 27 THz closely corresponding to two principal low-frequency peaks of EP. This exact local phonon mode coupling enhances ITC by simultaneously increasing phonon transmittance and widening the spectral bandwidth, available for interfacial heat transport.

As shown in Figure 5j, the TMSPA-functionalized interface achieves maximal vibrational coupling energy due to dense continuum of mid- to low-frequency modes aligned with the principal bands of EP, directly correlating with the significant enhancement in thermal conductivity observed experimentally. This superiority stems from the rigid aromatic amine group and planar benzene ring of TMSPA, which limit molecular mobility to create an ordered interface that optimizes vibrational coupling [60]. By contrast, the APTES shows moderate overlap energy limited by rotational freedom of its flexible primary amine group (NH_2), resulting in a disordered interface that reduces phonon transmission and ITC improvement. MPTMS shows the lowest overlap energy due to its long and compliant C—S bonds which weaken the vibrational coupling and contribute to a more disordered interface, leading to minimal ITC enhancement. These results establish the critical role of molecular interfacial structure in determining the VDOS and ITC of GF composites, where structural order directly governs phonon spectral matching efficiency and thermal conductance.

To elucidate the contributions of covalent bonding and non-bonded interactions to thermal conductance enhancement, the heat flux was decomposed along the transport axis and the energy components contributing to ITC were quantified (Figure 5k). At the TMSPA-functionalized interface, the contributions from the LJ and covalent bond interactions were 12.88 and 179.12 MW m^{-2} K^{-1}, respectively, significantly higher than those observed for APTES and MPTMS. The increased LJ contribution is attributed to the rigid, planar benzene ring structure, which reduces molecular conformational flexibility and enhances the packing density at the interface, thereby improving van der Waals non-bonded interactions. In parallel, the conjugated benzene ring geometry promotes efficient phonon coupling in the mid- to low-frequency range, reducing phonon scattering. The well-ordered covalent crosslinking facilitated by the benzene ring further establishes a continuous dense network, substantially increasing the bonded energy term. Collectively, these synergistic mechanisms maximize both non-bonded and bonded thermal pathways for phonon transportation, significantly boosting ITC in GF composites at molecularly engineered interfaces.

3 | Conclusions

This study established a molecular conjugation interface engineering strategy that resolves the fundamental interfacial incompatibility in GF composites. By covalently grafting benzene-ring-anchored silane tethers onto plasma-activated GF surfaces through a scalable manufacturing protocol, we achieved exceptional performance enhancements, exhibiting 61.6%, 34.9%, and 53.1% improvements in IFSS (89.2 MPa), ILSS (44.4 MPa) and tensile strength (68.8 MPa), respectively. The in-plane thermal conductivity increased by 34.6% to 571.1 W m^{-1} K^{-1} while maintaining >98% retention after thermal cycles testing, surpassing conventional CF composites. Concurrently, the composites achieved a 52.3% decrease in CTE while elevating the glass transition temperature by 27°C. The MD simulations reveal that π-electron-mediated phonon coupling at conjugated interfaces yields exceptional thermal conductance (373.56 MW m^{-2} K^{-1}), establishing directional transport channels that minimize phonon scattering. These multi-scale enhancements originate from atomic-scale conjugation and wrinkle-adaptive covalent networks that suppress interfacial delamination. This approach achieves synergistic mechanical-thermal enhancement in GF composites, enabling robust thermal management materials for extreme high-flux applications.

4 | Experimental Section

4.1 | Material

GFs (3000 filaments, thermal conductivity of 1204 ± 28 W m^{-1} K^{-1}, density of 1.93 ± 0.08 g cm^3) were prepared in our group through an established wet-spinning and thermal treatment process. Ethyl alcohol and three SCAs including: (3-Aminopropyl) triethoxysilane (APTES), trimethoxy [3-(phenylamino) propyl] silane (TMSPA) and (3-Mercaptopropyl) triethoxysilane (MPTMS) were provided by Aladdin Industry Co., Ltd. (Shanghai, China). Bisphenol A EP with an epoxy value of 51 and a curing agent, polyether amine (D-230), were obtained from Pugongying New Materials Co., Ltd. Suzhou China.

4.2 | Fabrication of SCA Modified GFs

Plasma treatment of GFs was conducted at 50 Pa and 90 W for 180 s, with the fiber samples suspended by metal clips to ensure uniformity, yielding oxygen-functionalized fibers (OGF). Functionalization involved immersing 1 g of OGF in 100 mL of a 3% silane coupling agent (SCA: APTES, TMSPA, or MPTMS) solution (ethanol/deionized water = 80:20, v/v) at 60°C for 2 h. The hydrolysis reaction was intentionally conducted without external pH adjustment, proceeding at the natural pH of the SCA solutions, which was measured approximately 9 (for APTES) and 5 (for TMSPA and MPTMS). Critically, all SCA solutions remained clear and stable without any precipitation or gelation throughout the 2 h reaction period (as validated in Figure S2). The fibers were then ethanol-washed, vacuum-dried at 80°C to constant weight, and labeled as OGF/N (amino), OGF/Ph (phenylamino), or OGF/S (sulfhydryl).

4.3 | Fabrication of GF Composites

For composite preparation, the functionalized GFs were ultrasonically cleaned in ethanol (3 min), dried at 60°C (30 min), and aligned in a Teflon mold. An epoxy matrix (E51:D230 = 100:33 mass ratio) was mechanically stirred (10 min), vacuum-degassed (0.1 MPa, 20 min), and infused into the mold under 0.1 MPa. The

16163028, 0, Downloaded from https://advanced.onlinelibrary.wiley.com/doi/10.1002/adfm.202522804 by Zhejiang University, Wiley Online Library on [07/04/2026]. See the Terms and Conditions (https://onlinelibrary.wiley.com/terms-and-conditions) on Wiley Online Library for rules of use; OA articles are governed by the applicable Creative Commons License

assembly was hot-pressed at 60°C with pressure ramping from 5 to 30 MPa over 4 h, achieving fiber volume fractions of 20%–60%.

Author Contributions

X.Y.F., W.W.L., and G.D.W. contributed equally to this work. **X. Ming**, **X. Y. Feng**, and **J. Y. Liu** conceived the research. **X. Y. Feng** and **X. Ming** designed experiments, analyzed the data, and wrote the manuscript. **B. Wang**: prepared for the graphene fibers. **L. Chen** and **S. Q. Wu** conducted SEM imaging on the sample. **L. He**, **P. X. Zhou**, and **C. D. Ge** did the mechanical test of samples. **J. H. Lu** assisted the electrical and thermal test of samples. **G. D. Wu** and **L. Qiu** conducted MD simulation analysis. **Z. Xu** and **Z. Z. Yu** discussed the design of experiments. **X. Ming**, **J. Y. Liu**, **W. F. Shen**, **J. G. Tang**, **L. Qiu**, and **C. Gao** supervised the project.

Acknowledgements

This work was supported by the Natural Science Foundation of Zhejiang Province (LR23E020003), National Natural Science Foundation of China (Nos. 52272046, 52090030, 52090031, 52122301, 51973191, 52222602, 52476052), National Key Research and Development (R&D) Program of China (NO. 2022YFA1205300, NO. 2022YFA1205301), Natural Science Foundation of Shandong Province (Grant No. ZR2024ME198), State Key Project of International Cooperation Research (2023YFE0201100), "Pioneer" and "Leading Goose" R&D Program of Zhejiang (2026C02A1055, 2023C01190), Shanxi-Zheda Institute of New Materials and Chemical Engineering (2022SZ-TD011, 2022SZ-TD012), Xinmiao Talents Program of Zhejiang Province (2023R401193) and the Fundamental Research Funds for the Central Universities (226-2025-00219).

Conflicts of Interest

The authors declare no conflict of interest.

Data Availability Statement

The data that support the findings of this study are available from the corresponding author upon reasonable request.

References

1. Z. Xu and C. Gao, "Graphene Chiral Liquid Crystals and Macroscopic Assembled Fibres," *Nature Communications* 2 (2011): 571.

2. P. Li, Z. Wang, Y. Qi, et al., "Bidirectionally Promoting Assembly Order for Ultrastiff and Highly Thermally Conductive Graphene Fibres," *Nature Communications* 15 (2024): 409.

3. P. Li, Y. Liu, S. Shi, et al., "Highly Crystalline Graphene Fibers With Superior Strength and Conductivities by Plasticization Spinning," *Advanced Functional Materials* 30 (2020): 2006584.

4. Y. Liu, Z. Xu, J. Zhan, P. Li, and C. Gao, "Superb Electrically Conductive Graphene Fibers via Doping Strategy," *Advanced Materials* 28 (2016): 7941–7947.

5. B. Fang, D. Chang, Z. Xu, and C. Gao, "A Review on Graphene Fibers: Expectations, Advances, and Prospects," *Advanced Materials* 32 (2020): 1902664.

6. X. Ming, A. Wei, Y. Liu, et al., "2D-Topology-Seeded Graphitization for Highly Thermally Conductive Carbon Fibers," *Advanced Materials* 34 (2022): 2201867.

7. H. Zhang, A. Li, J. Wu, and D. Yang, "Multi-Material 3D Printing of Continuous Carbon Fibre Reinforced Thermoset Composites With Tailored Fibre Paths and Bespoke Conforming Thermoplastic Moulds," *Composites Part B: Engineering* 298 (2025): 112373.

8. S. Saad, A. S. Zeraati, S. Roy, et al., "Transformation of Petroleum Asphaltenes to Carbon Fibers," *Carbon* 190 (2022): 92–103.

9. G. Ye, H. Wu, K. Shi, et al., "Preparation of Continuous Large-Diameter Mesophase Pitch-Based Carbon Fiber With Good Weavability and Potential Ultra-High Thermal Conductivity," *Carbon* 238 (2025): 120181.

10. S. Liu, Y. Wang, X. Ming, Z. Xu, Y. Liu, and C. Gao, "High-Speed Blow Spinning of Neat Graphene Fibrous Materials," *Nano Letters* 21 (2021): 5116–5125.

11. H. Shi, B. Wang, L. Wang, et al., "Large-Scale Preparation of Thermally Conductive Graphene Fiber Filaments," *Carbon* 221 (2024): 118947.

12. J. Hong, D.-W. Park, and S. E. Shim, "A Review on Thermal Conductivity of Polymer Composites Using Carbon-Based Fillers : Carbon Nanotubes and Carbon Fibers," *Carbon Letters* 11 (2010): 347–356.

13. N. Sun, B. Lin, Q. Cui, et al., "In Situ Construction of Vertical Carbon Nanosheets on Carbon Fibers Toward High-Performance Epoxy Composites via Interfacial Enhancement," *Chemical Engineering Journal* 524 (2025): 169702.

14. S.-C. Zhang, X.-H. Lu, J. Liu, et al., "A Biomimetic Thermal Conduction Network Enables Metal-Level Thermal Conductivity in Polymer Nanocomposites," *ACS Nano* 19 (2025): 36663–36674.

15. X. Lu, J. Liu, C. Shu, et al., "Densifying Conduction Networks of Vertically Aligned Carbon Fiber Arrays With Secondary Graphene Networks for Highly Thermally Conductive Polymer Composites," *Advanced Functional Materials* 35 (2025): 2417324.

16. L. Zhou, X. Liu, T. Li, and Y. Lu, "Engineering Rigid-Flexible Interfacial Structure in Carbon Fiber-Reinforced Composites via Mussel-Inspired Chemistry-Assisted RAFT Polymerization," *Composites Part B: Engineering* 304 (2025): 112644.

17. D. An, H. Chen, H. Yu, et al., "Improving Electromagnetic Engineering of Thermal Conductive Composites by Establishing Continuous Thermal Conductive Networks With Gradient Impedance," *Journal of Materials Chemistry C* 13 (2025): 1646–1657.

18. D. An, Y. Cui, R. He, et al., "Improved Interfacial Interactions of Modified Graphene Oxide/Natural Rubber Composites With the Low Heat Build-Up and Good Mechanical Property for the Green Tire Application," *Polymer Composites* 46 (2025): 1024–1036.

19. D. An, H. Chen, R. He, et al., "MOF Decorated Boron Nitride/Natural Rubber Composites With Heterostructure for Thermal Management Application Through Dual Passive Cooling Modes Base on the Improved Thermal Conductivity and Water Sorption-Desorption Process," *Composites Science and Technology* 248 (2024): 110469.

20. H. Zhang, Q. He, F. Zhang, Y. Duan, M. Qin, and W. Feng, "Biomimetic Intelligent Thermal Management Materials: From Nature-Inspired Design to Machine-Learning-Driven Discovery," *Advanced Materials* 37 (2025): 2503140.

21. J. Yue, M. Qin, H. Yu, Q. He, and W. Feng, "Superelastic Graphene-Based Composite Aerogel for Thermal and Electromagnetic Protection in Extreme Temperature Environments," *Advanced Functional Materials* 35 (2025): 2508319.

22. Y. Zhang, J. Yang, R. Xu, M. Liu, Y. Liu, and J. Wang, "Investigation of Anisotropic Thermophysical Properties of Highly Oriented Carbon Fiber Composites: From One to Three Dimensions," *Carbon* 243 (2025): 120477.

23. J. Zhou, Z. Song, J. Wan, et al., "Polyaniline-Functionalized MoS2 Nanosheets/Carbon Fiber Network for Structural and Functional Integration of Composites," *Composites Part B: Engineering* 306 (2025): 112847.

24. J. Luo, Y. Xue, X. Yang, et al., "Integrating Thermal, EMI Shielding, and Mechanical Properties in Carbon Fiber/Epoxy Resin Composites via Interface-Layup Synergistic Design," *Advanced Functional Materials* (2025): 13660.

25. Z. Xu, H. Sun, X. Zhao, and C. Gao, "Ultrastrong Fibers Assembled From Giant Graphene Oxide Sheets," *Advanced Materials* 25 (2013): 188–193.

16163028, 0, Downloaded from https://advanced.onlinelibrary.wiley.com/doi/10.1002/adfm.202522804 by Zhejiang University, Wiley Online Library on [07/04/2026]. See the Terms and Conditions (https://onlinelibrary.wiley.com/terms-and-conditions) on Wiley Online Library for rules of use; OA articles are governed by the applicable Creative Commons License

26. Q. Tian, Z. Xu, Y. Liu, et al., "Dry Spinning Approach to Continuous Graphene Fibers With High Toughness," *Nanoscale* 9 (2017): 12335–12342.

27. J. Lu, X. Ming, M. Cao, et al., "Scalable Compliant Graphene Fiber-Based Thermal Interface Material With Metal-Level Thermal Conductivity via Dual-Field Synergistic Alignment Engineering," *ACS Nano* 18 (2024): 18560–18571.

28. Q. Yin, B. Wang, G. Cai, et al., "Highly Thermally Conductive Composites of Graphene Fibers," *Composites Part A: Applied Science and Manufacturing* 185 (2024): 108290.

29. X. Shen, Z. Wang, Y. Wu, et al., "A Three-Dimensional Multilayer Graphene Web for Polymer Nanocomposites With Exceptional Transport Properties and Fracture Resistance," *Materials Horizons* 5 (2018): 275–284.

30. A. Nag, M. E. E. Alahi, and S. C. Mukhopadhyay, "Recent Progress in the Fabrication of Graphene Fibers and Their Composites for Applications of Monitoring Human Activities," *Applied Materials Today* 22 (2021): 100953.

31. F. Wang, W. Fang, X. Ming, Y. Liu, Z. Xu, and C. Gao, "A Review on Graphene Oxide: 2D Colloidal Molecule, Fluid Physics, and Macroscopic Materials," *Applied Physics Reviews* 10 (2023): 011311.

32. P. Zhang, Y. Hao, H. Shi, et al., "Highly Thermally Conductive and Structurally Ultra-Stable Graphitic Films With Seamless Heterointerfaces for Extreme Thermal Management," *Nano-Micro Letters* 16 (2024): 58.

33. L. Ding, T. Xu, J. Zhang, et al., "Covalently Bridging Graphene Edges for Improving Mechanical and Electrical Properties of Fibers," *Nature Communications* 15 (2024): 4880.

34. H. Xu, X. Zhang, D. Liu, et al., "Cyclomatrix-Type Polyphosphazene Coating: Improving Interfacial Property of Carbon Fiber/Epoxy Composites and Preserving Fiber Tensile Strength," *Composites Part B: Engineering* 93 (2016): 244–251.

35. Z. Sun, Y. Luo, C. Chen, et al., "Mechanical Enhancement of Carbon Fiber-Reinforced Polymers: From Interfacial Regulating Strategies to Advanced Processing Technologies," *Progress in Materials Science* 142 (2024): 101221.

36. F. Liu, Z. Shi, and Y. Dong, "Improved Wettability and Interfacial Adhesion in Carbon Fibre/Epoxy Composites via An Aqueous Epoxy Sizing Agent," *Composites Part A: Applied Science and Manufacturing* 112 (2018): 337–345.

37. W. Han, H.-P. Zhang, J. Tavakoli, J. Campbell, and Y. Tang, "Polydopamine as Sizing on Carbon Fiber Surfaces for Enhancement of Epoxy Laminated Composites," *Composites Part A: Applied Science and Manufacturing* 107 (2018): 626–632.

38. H. Zhang and W. Li, "Plasma-Grafting Polymerization on Carbon Fibers and Its Effect on Their Composite Properties," *Applied Surface Science* 356 (2015): 492–498.

39. M. Felisberto, L. Tzounis, L. Sacco, et al., "Carbon Nanotubes Grown on Carbon Fiber Yarns by a Low Temperature CVD Method: A Significant Enhancement of the Interfacial Adhesion Between Carbon Fiber/Epoxy Matrix Hierarchical Composites," *Composites Communications* 3 (2017): 33–37.

40. S.-J. Park and J.-S. Jin, "Effect of Silane Coupling Agent on Interphase and Performance of Glass Fibers/Unsaturated Polyester Composites," *Journal of Colloid and Interface Science* 242 (2001): 174–179.

41. Z. Wen, C. Xu, X. Qian, et al., "A Two-Step Carbon Fiber Surface Treatment and Its Effect on the Interfacial Properties of CF/EP Composites: The Electrochemical Oxidation Followed by Grafting of Silane Coupling Agent," *Applied Surface Science* 486 (2019): 546–554.

42. X. Li, S. Liu, X. Meng, et al., "Modified Antistatic Carbonaceous Fiber With Excellent Hydrophobicity, Environmental Stability and Radar Absorption Performance," *Carbon* 229 (2024): 119501.

43. Y. Wu, D. Dhamodharan, Z. Wang, R. Wang, and L. Wu, "Effect of Electrophoretic Deposition Followed by Solution Pre-Impregnated Surface Modified Carbon Fiber-Carbon Nanotubes on the Mechanical Properties of Carbon Fiber reinforced Polycarbonate Composites," *Composites Part B: Engineering* 195 (2020): 108093.

44. Q. Zhai, Z. Lu, J. Wang, et al., "Hydrolysis Kinetics of Silane Coupling Agents Studied by Near-Infrared Spectroscopy Plus Partial Least Squares Model," *Phosphorus, Sulfur, and Silicon and the Related Elements* 194 (2019): 803–811.

45. M. Baghery Borooj, A. Mousavi Shoushtari, A. Haji, and E. Nosratian Sabet, "Optimization of Plasma Treatment Variables for the Improvement of Carbon Fibres/Epoxy Composite Performance by Response Surface Methodology," *Composites Science and Technology* 128 (2016): 215–221.

46. S. Li, X. Li, M. Shao, et al., "Regulating Interfacial Compatibility With Amino Silane and Bio-Inspired Polydopamine for High-Performance Epoxy Composites," *Tribology International* 140 (2019): 105861.

47. K. Beak, M. Choi, D. H. Kim, et al., "Silane-Treated BaTiO3 Ceramic Powders for Multilayer Ceramic Capacitor With Enhanced Dielectric Properties," *Chemosphere* 286 (2022): 131734.

48. Y. Nakaramontri, C. Kummerlöwe, C. Nakason, and N. Vennemann, "The Effect of Surface Functionalization of Carbon Nanotubes on Properties of Natural Rubber/Carbon Nanotube Composites," *Polymer Composites* 36 (2015): 2113–2122.

49. Y. Li, L. Zhang, and C. Li, "Highly Transparent and Scratch Resistant Polysiloxane Coatings Containing Silica Nanoparticles," *Journal of Colloid and Interface Science* 559 (2020): 273–281.

50. R. Radjef, K. L. Jarvis, B. L. Fox, and S. L. McArthur, "Comparing the Properties of Commercially Treated and Air Plasma Treated Carbon Fibers," *Surface and Coatings Technology* 408 (2021): 126751.

51. Z. Chen, Q. Tu, X. Shen, et al., "Enhancing the Thermal and Mechanical Properties of Carbon Fiber/Natural Rubber Composites by Co-Modification of Dopamine and Silane Coupling Agents," *Polymer Testing* 126 (2023): 108164.

52. F. M. Monticeli, J. H. S. Almeida Jr, R. M. Neves, F. G. Ornaghi, and H. L. Ornaghi, "On the 3D Void Formation of Hybrid Carbon/Glass Fiber Composite Laminates: A Statistical Approach," *Composites Part A: Applied Science and Manufacturing* 137 (2020): 106036.

53. F. M. Monticeli, H. L. Ornaghi, H. J. Cornelis Voorwald, and M. O. H. Cioffi, "Three-Dimensional Porosity Characterization in Carbon/Glass Fiber Epoxy Hybrid Composites," *Composites Part A: Applied Science and Manufacturing* 125 (2019): 105555.

54. J. Lin, C. Sun, J. Min, H. Wan, and S. Wang, "Effect of Atmospheric Pressure Plasma Treatment on Surface Physicochemical Properties of Carbon Fiber Reinforced Polymer and Its Interfacial Bonding Strength With Adhesive," *Composites Part B: Engineering* 199 (2020): 108237.

55. J. Li, B. Zhang, X. Zhang, et al., "Revolutionizing High-Temperature Electrical Properties of Epoxy Resin via Tailoring Weak Conjugation Rigid Structures (Small 11/2025)," *Small* 21 (2025): 2570084.

56. T. H. Lee, Y. I. Park, S. M. Noh, and J. C. Kim, "In-Situ Visualization of the Kinetics of Low Temperature Thiol-Epoxy Cross-Linking Reactions by Using a pH-Responsive Epoxy Resin," *Progress in Organic Coatings* 104 (2017): 20–27.

57. X. Wu, J. Zhao, X. Rao, and D. D. L. Chung, "Carbon Fiber Epoxy-Matrix Composites With Hydrothermal-Carbon-Coated Halloysite Nanotube Filler Exhibiting Enhanced Strength and Thermal Conductivity," *Polymer Composites* 41 (2020): 2687–2703.

58. K. Dong, J. Zhang, M. Cao, M. Wang, B. Gu, and B. Sun, "A Mesoscale Study of Thermal Expansion Behaviors of Epoxy Resin and Carbon Fiber/Epoxy Unidirectional Composites Based on Periodic Temperature and Displacement Boundary Conditions," *Polymer Testing* 55 (2016): 44–60.

59. J. Liu, M. Alhashme, and R. Yang, "Thermal Transport Across Carbon Nanotubes Connected by Molecular Linkers," *Carbon* 50 (2012): 1063–1070.

16163028, 0, Downloaded from https://advanced.onlinelibrary.wiley.com/doi/10.1002/adfm.202522804 by Zhejiang University, Wiley Online Library on [07/04/2026]. See the Terms and Conditions (https://onlinelibrary.wiley.com/terms-and-conditions) on Wiley Online Library for rules of use; OA articles are governed by the applicable Creative Commons License

60. X. Huang, S. Ma, C. Y. Zhao, H. Wang, and S. Ju, "Exploring High Thermal Conductivity Polymers via Interpretable Machine Learning With Physical Descriptors," *npj Computational Materials* 9 (2023): 191.

Supporting Information

Additional supporting information can be found online in the Supporting Information section.

Supporting File: adfm73778-sup-0001-SuppMat.docx.

16163028, 0, Downloaded from https://advanced.onlinelibrary.wiley.com/doi/10.1002/adfm.202522804 by Zhejiang University, Wiley Online Library on [07/04/2026]. See the Terms and Conditions (https://onlinelibrary.wiley.com/terms-and-conditions) on Wiley Online Library for rules of use; OA articles are governed by the applicable Creative Commons License